

See discussions, stats, and author profiles for this publication at: <https://www.researchgate.net/publication/257531608>

# Ultrafast Shock Initiation of Exothermic Chemistry in Hydrogen Peroxide

ARTICLE *in* THE JOURNAL OF PHYSICAL CHEMISTRY A · OCTOBER 2013

Impact Factor: 2.69 · DOI: 10.1021/jp407595u · Source: PubMed

CITATIONS

7

READS

59

11 AUTHORS, INCLUDING:



[Joseph M Zaug](#)

Lawrence Livermore National Laboratory

120 PUBLICATIONS 1,186 CITATIONS

SEE PROFILE



[Nir Goldman](#)

Lawrence Livermore National Laboratory

65 PUBLICATIONS 1,184 CITATIONS

SEE PROFILE



[Michaela Kashgarian](#)

Lawrence Livermore National Laboratory

65 PUBLICATIONS 2,672 CITATIONS

SEE PROFILE



[Troy Barbee](#)

Lawrence Livermore National Laboratory

474 PUBLICATIONS 5,840 CITATIONS

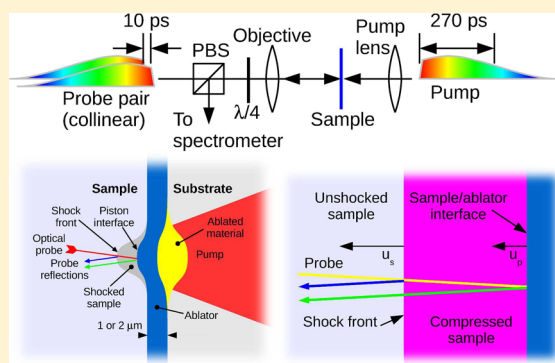
SEE PROFILE

# Ultrafast Shock Initiation of Exothermic Chemistry in Hydrogen Peroxide

Michael R. Armstrong,\* Joseph M. Zaug,<sup>†</sup> Nir Goldman, I-Feng W. Kuo, Jonathan C. Crowhurst, W. Michael Howard, Jeffrey A. Carter, Michaele Kashgarian, John M. Chesser, Troy W. Barbee, and Sorin Bastea

Physical and Life Sciences Directorate, Lawrence Livermore National Laboratory, Livermore, California 94550, United States

**ABSTRACT:** We report observations of shock compressed, unreacted hydrogen peroxide at pressures up to the von Neumann pressure for a steady detonation wave, using ultrafast laser-driven shock wave methods. At higher laser drive energy we find evidence of exothermic chemical reactivity occurring in less than 100 ps after the arrival of the shock wave in the sample. The results are consistent with our MD simulations and analysis and suggest that reactivity in hydrogen peroxide is initiated on a sub-100 ps time scale under conditions found just subsequent to the lead shock in a steady detonation wave.



## 1. INTRODUCTION

Shock wave initiated chemistry is an essential condition for the detonation of chemical explosives<sup>1,2</sup> and has great potential for exploring nonequilibrium material synthesis.<sup>3,4</sup> However, the physical and chemical processes that occur at a shock wavefront are still not fully understood.<sup>5–8</sup> Shock waves can change the thermodynamic state of a material over picosecond time scales<sup>9</sup> (i.e., faster than the time scale of quasi-equilibrium reaction kinetics for many reactive systems), but traditional experiments in detonation chemistry have not had the time resolution (typically greater than 1 ns) to observe chemistry over the duration of a shock wave rise.<sup>9,10</sup>

Although nanosecond resolution experiments generate the same shocked thermodynamic states and compressive strain rates as picosecond scale experiments, such experiments cannot observe phenomena on the scale of the lead shock or, in the case of the steady detonation of hydrogen peroxide, the von Neumann spike. In particular, longer time scale experiments typically observe apparent strain rates no greater than  $10^7 \text{ s}^{-1}$ , where strain rates at the lead shock in a liquid might exceed  $10^{10} \text{ s}^{-1}$ , at least 3 orders of magnitude larger. Ultimately, in the absence of experiments at the time scale of shock compression, the specific assumptions of phenomenological models (and extrapolations therein) over these time scales remain a matter of speculation.

For instance, it remains a matter of debate whether high strain rate compression at a shock wavefront can lead to nonequilibrium, strain rate dependent chemistry, “mechanochemistry”, as proposed by Gilman et al.<sup>11,12</sup> Standard kinetic models of detonation do not take into account such nonequilibrium effects and assume that chemical reactions are spontaneously initiated solely due to local thermodynamic

conditions,<sup>13</sup> but they have not been experimentally verified on the time scale of the lead shock. In other systems, high strain rate behavior can vary substantially from what is observed in long time scale, low time resolution experiments.<sup>10</sup>

Here, we experimentally and theoretically investigate shock wave compressed hydrogen peroxide at pressures up to the von Neumann pressure for a steady detonation. Hydrogen peroxide ( $\text{H}_2\text{O}_2$ ) is a model reactive system under shock loading where mixtures with and without water are known to detonate.<sup>14</sup> Gas gun studies have indicated microsecond time scales for its reactivity under shock compression,<sup>2</sup> in sharp contrast to the picosecond time scales observed in simulations for similar hydrides (e.g.,  $\text{H}_2\text{O}$ <sup>6,15</sup>). In this work we experimentally study the behavior of  $\text{H}_2\text{O}_2$  on picosecond time scales using ultrafast shock wave characterization techniques.<sup>10,16–20</sup>

Our high time resolution ( $\sim 10 \text{ ps}$ ) experiments indicate that exothermic chemical reactions in hydrogen peroxide begin within 100 ps subsequent to shock compression, at a compressive strain rate (at the piston) of at least  $10^{10} \text{ s}^{-1}$ . We also present molecular dynamics simulations that predict reactivity in a steady detonation wave on a sub-100 ps time scale, corroborating the experimental results. Owing to the short time scale of the experiments (which have a total duration of  $\sim 250 \text{ ps}$ ), we obtain information relevant principally to shock initiation of exothermic chemistry just subsequent to the lead shock. Though hydrogen peroxide is known to detonate, the time scale of our experiments is not sufficient to observe a steady detonation wave. Nevertheless, our experiment achieves

Received: July 30, 2013

Revised: October 2, 2013

Published: October 8, 2013

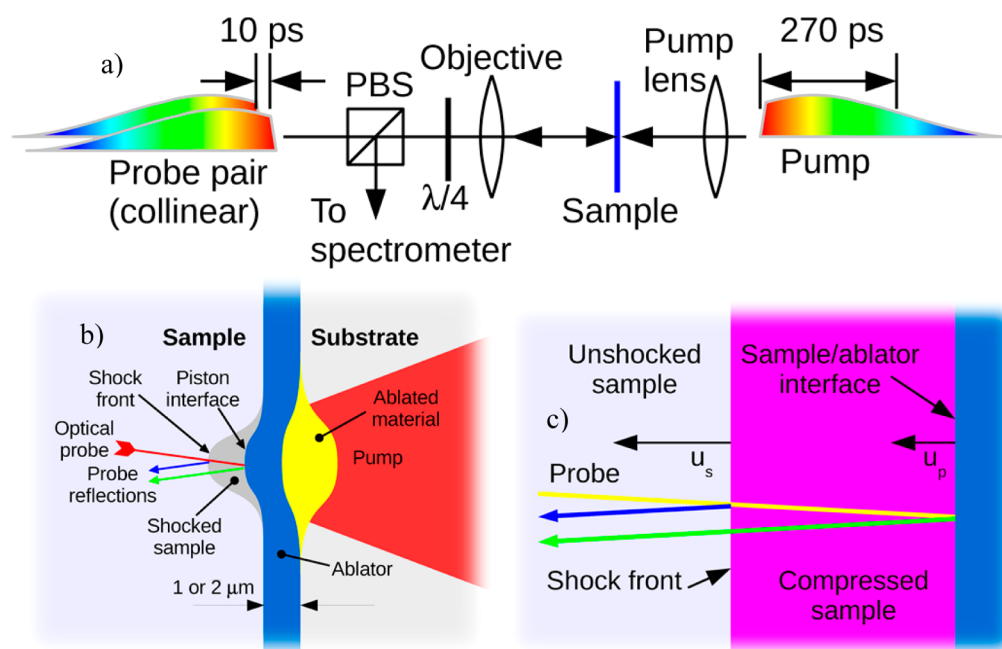


**Figure 1.** Scheme for shock loading  $\text{H}_2\text{O}_2$ . (a) Chirped pump and probes are incident on the sample from opposite sides. PBS stands for polarizing beam splitter and  $\lambda/4$  is a quarter waveplate set to rotate the polarization  $90^\circ$  in the double pass. (b) The pump ablates a metal layer on a glass substrate, driving a shock wave into the hydrogen peroxide sample (starting from ambient pressure and temperature). (c) Probe reflections from the shock front and the sample/ablator interface are Doppler shifted to different frequencies. To simplify the illustration, only two reflections are shown. Here,  $u_s$  is the speed of the shock front and  $u_p$  is the piston speed.

a pressure and density consistent with the von Neumann pressure at the lead shock, providing a window into the process of initiation for a steady detonation.

## 2. EXPERIMENTAL DETAILS

### a. Generation and Characterization of Shock Waves.

The method we have used for generating shock compression and characterizing the shocked state of the material<sup>10,16</sup> yields the thermodynamic state of the shocked sample via measurements of shock wave and piston speeds, analogous to longer time scale experiments, but here we obtain  $\sim 10$  ps time resolution. A parametrized fit to the raw data gives the piston and shock wave speeds (see below) after which the pressure and density of the shocked state are calculated via the Rankine–Hugoniot jump conditions.<sup>21</sup>

The experimental setup is shown in Figure 1. A shaped pump pulse<sup>22</sup> with approximately 270 ps duration, 20  $\mu\text{m}$  diameter, and 800 nm wavelength with a  $\sim 12$  ps rise time is focused with a 2 cm focal length lens onto a 1 or 2  $\mu\text{m}$  thick metal ablation layer coated on a  $\sim 100$   $\mu\text{m}$  thick glass substrate (i.e., a coverslip). This generates a rapidly expanding plasma that drives a shock wave into the metal layer and subsequently into the sample as shown in Figure 1b. Meanwhile, a collinear pair of time delayed and chirped probe pulses each of the same duration as the pump (but with much lower energy) reflect from the opposite side of the sample and are imaged onto the slit of a spectrometer with a 0.28 NA microscope objective, with 10 $\times$  total magnification between the sample and the spectrometer. Via the Doppler effect, the motion of the shock front and the ablator/sample interface shifts the frequency of corresponding reflections to different frequencies; two such reflections are shown in Figure 1b,c. The average frequency of the reflected probe is increased (because all interfaces are moving in the direction opposite the incident probe), and

frequency components reflected from the shock and piston (i.e., ablator/sample interface) beat against each other. Our diagnostic measures a finite time derivative of the phase, which is proportional to frequency shifts. For constant shock and piston velocities, the resulting signal comprises an offset from the baseline, which corresponds to the average frequency shift, plus an oscillation, which corresponds to beating between shock and piston reflections. From fits to the data, three parameters: the offset, and the period and amplitude of the oscillation, give the shock velocity, the piston velocity, and the index of refraction of the shocked material. See ref 16 for complete details.

Because the probe pulses are chirped there is a monotonic correlation between the wavelength and time delay within the pulse, and the phase shift is thus measured as a function of time in a single shot,<sup>16,18</sup> which is convenient because each shot is locally destructive. A fast rise in the pump pulse temporal profile (required to obtain a fast shock rise time in the ablator) is formed by clipping the spectral profile of the chirped pulse in a pulse stretcher, consistent with ref 17. Although the profile over a one-dimensional spatial cut through the center of the shocked region is obtained (corresponding to position along the slit of the spectrometer), only the center of this profile (i.e., the center of the ablation spot) is analyzed for each shot.

For the two data clusters at  $\sim 2$  km/s effective piston speed (see below), a 1  $\mu\text{m}$  ablator is used with two different pump energies, where the peak intensity for the higher shock speed cluster is  $\sim 10^{11}$  W/cm<sup>2</sup> (corresponding to a pump energy of about 100  $\mu\text{J}$ ), and the pulse energy for the lower shock speed cluster was approximately 22% lower. Due to a high numerical aperture for the pump focus, the exact intensity is difficult to specify, but the energy difference between the two clusters is very well characterized, because it is determined by a more precise adjustment of the pump energy. For the set of shots

with piston speeds around 1.2 km/s, a 2  $\mu\text{m}$  ablator is used to obtain a lower piston speed. Variation of the average piston speed for a given data cluster is due to variation of the sample position along the optical axis between different shots, which slightly changes the focal spot size, and the intensity, between shots. Thus each data cluster samples a range of piston speeds.

**b. Data Analysis.** All data were analyzed using the method of ref 16. As described above, the raw data consisted of a sinusoidal oscillation offset from the baseline. Shock and piston speeds were determined via estimates of the period and amplitude of the oscillation, and the offset. All data in this work were fit to a sinusoid plus a linear function, where the slope and offset of the linear function and the phase, amplitude, and period of the sinusoid were fitting parameters. The offset used to estimate velocities was the average of the linear part of the fit function within the fitting window.

**c. Sample Preparation.** The sample was 90% hydrogen peroxide by weight mixed with water. High test  $\text{H}_2\text{O}_2$  was purchased from FMC Industrial Chemicals. Average peroxide concentrations were determined by measuring the index of refraction (293 K on a temperature controlled stage) with an Atago RX-5000a refractometer (sapphire prisms). We utilized the peroxide concentration calibration established by Giguère and Geoffrion.<sup>23</sup> The refractometer was calibrated using Cargille refractive index (matching) liquids at the sodium D-line wavelength of 589 nm. Average densities were determined from five mass measurements of nominally 100  $\mu\text{L}$  aliquots each contained in passivated and tared borosilicate glass shell vials. Aliquots were drawn with a calibrated positive displacement micropipet (Gilson M100) and weighed on a Mettler analytical balance.

**d. Ablators.** Ablators consisted of alternating layers of 46 nm Al and 1.5 nm Ti to total thicknesses of 1 and 2  $\mu\text{m}$ , coated on a #1 borosilicate glass coverslip window. Al/Ti multilayer films were substantially smoother than pure Al films of comparable thickness,<sup>24,25</sup> typically 2 nm  $\pm$  1 nm RMS roughness. The probe side window was a 1 mm thick glass window with an 800 nm antireflection coating on the air side and no coating on the sample side. A 125  $\mu\text{m}$  thick Teflon gasket radially confined the peroxide fluid, at ambient conditions, between the two parallel facing windows. All surfaces exposed to hydrogen peroxide were passivated for 24–48 h in 90% hydrogen peroxide. Although some small bubbles formed from decomposition of the sample while the data were acquired (over some hours), these were not enough to significantly change the concentration of the sample.

**e. Analysis of Uncertainties in Shock Wave Data.** The data were analyzed at varying fit window positions and the speed results did not vary outside the scatter of the data (for a given cluster) as a function of the fitting window position. The distance over which the shock wave travels during the experiment was less than 1% of the radius of curvature of the wavefront, so the error in shock wave speed estimates due to nonplanarity of the wavefront was much smaller than other errors in the experiment,<sup>26</sup> consistent with previous work described in refs 10 and 16. All estimates of wave speeds were taken at the center of the shock wave spatial profile, so errors due to off-normal-axis components of the wave velocity were also negligible.

The method measured the piston speed, which in general might not be the same as the particle speed just behind the shock front. To determine the error in assuming the particle speed to be equal to the measured average piston speed, we

simulated the hydrodynamics of shock wave propagation in water assuming piston speed boundary conditions with worst-case forms found in the measured data, using ALE3D,<sup>27</sup> and then derived a simulated signal from the results of the hydrodynamics simulations. The simulated signal was analyzed using the same method we used to analyze actual data. From this analysis, the estimated shock wave speed (from the simulations, at the estimated piston speed) differed from the Hugoniot by an amount that was less than the scatter in the data (see below).

**f. Sound Speed Measurements.** To validate the unreacted Hugoniot for comparison with the measured ultrafast data, it was necessary to determine the pressure dependence of the adiabatic speed of sound of concentrated  $\text{H}_2\text{O}_2$  (see below), collected along a 298 K isotherm. These were measured using the laser-based impulsive stimulated light scattering method, ISLS (e.g., ref 28), where a glass reference material with a well-characterized velocity was used to calibrate the sound speed measurement. Sound velocities were measured up to 2.48 GPa with samples compressed in a diamond anvil cell. The 89% concentrated peroxide fluid froze at a pressure between 1.74 and 2.07 GPa. The pressure was reduced from 2.48 to 1.23 GPa and the corresponding fluid-state velocity matched, within experimental error, our pre-established (initial compression cycle) 298 K isothermal results. Pressure was determined before and after each velocity measurement using the SrB calibration. Pressure and velocity measurement precisions were  $<\pm 0.03$  GPa and  $<1\%$ , respectively. Collecting elevated temperature data ( $T > 700$  K) was prohibited by rapid oxidation of the Ta gasket. Thermally robust alloy or pure metal gasket materials, e.g., Inconel, Re, Ir, rapidly decomposed  $\text{H}_2\text{O}_2$ .

For sound speed measurements at room temperature, samples were pressurized using a LLNL symmetric diamond-anvil cell (DAC) actuated by a pressurized metal membrane. Diamond-anvils (Type-I 400  $\mu\text{m}$  culet) and sample-retaining gaskets (250  $\mu\text{m}$  thick tantalum foil indented to 50  $\mu\text{m}$ ) were passivated using 90%  $\text{H}_2\text{O}_2$  ( $\sim 24$ –48 h) prior to sample loading. Tantalum and diamond were found to be inert (no oxygen bubbles formed during experiments). A  $\sim 10$   $\mu\text{L}$  liquid drop of  $\text{H}_2\text{O}_2$ ,  $\text{SrB}_4\text{O}_7\text{:Sm}^{2+}$  (SrB), and annealed cubic boron nitride (cBN) and pressure sensors (fluorescence and Raman respectively) were sealed into a DAC sample chamber. Raman measurements were conducted to monitor the sample cavity for the presence of oxygen, a clear indicator of peroxide decomposition. For the Raman measurements, the sample was illuminated with 488 nm light at  $<6$  mW power and a probe spot-size of approximately 10  $\mu\text{m}$ . Collected  $\mu$ -Raman spectra (30 s acquisitions) revealed no indication of the oxygen vibron. The pressure was determined before and after each velocity measurement using the most intense fluorescence peak line shift of  $\text{SrB}_4\text{O}_7\text{:Sm}^{2+}$  and the room temperature calibration established by Datchi et al.<sup>29</sup>

### 3. MOLECULAR DYNAMICS SIMULATIONS

Molecular dynamics (MD) simulations provide an independent route to equation of state data and also elucidate changes in phase or chemical speciation that occur during dynamic compression. Simulating the breaking and forming of chemical bonds behind a shock front frequently requires the use of a quantum theory.<sup>30</sup> The density functional tight binding method (DFTB) holds promise as a semiempirical quantum approach for simulations of materials at high pressures and temperatures.



DFTB (with self-consistent atomic charges) is an approximate quantum simulation technique that allows for several orders of magnitude increase in computational efficiency while retaining most of the accuracy of standard quantum simulations, (e.g., Kohn–Sham density functional theory<sup>31</sup>). This allows DFTB simulations to achieve close to equilibrium time-scales for long-time scale reactivity (e.g., several hundred picoseconds or greater<sup>6</sup>), whereas DFT-MD calculations are generally limited to tens of picoseconds<sup>15</sup> and can be far from equilibrium under similar conditions. DFTB has been shown to provide accurate descriptions of chemical reactivity for a number of systems under extreme conditions, including nitromethane<sup>5</sup> and HMX.<sup>32</sup>

DFTB force and stress tensor calculations were performed using the DFTB+ code (see refs 33 and 34) and the mio-0-1 parameter set (available for download from <http://www.dftb.org>). All DFTB calculations were driven by the LAMMPS molecular software simulation code,<sup>35</sup> and were calibrated against Kohn–Sham DFT calculations performed with the CP2K molecular simulation software suite.<sup>36</sup> CP2K uses a mixed planewave/Gaussian basis set and the Born–Oppenheimer approximation to maintain the system in its electronic ground state. For our purposes, we used a planewave cutoff of 400 Ry and an optimized triple- $\zeta$  valence polarized basis set for hydrogen and oxygen. We employed Goedecker–Teter–Hutter pseudopotentials<sup>37</sup> with the Becke–Lee–Yang–Parr exchange–correlation functional (see refs 38 and 39). Standard DFT methods strongly underestimated dispersion (van der Waals) interactions in many materials, resulting in an underestimation of the density under ambient conditions.<sup>40</sup> Currently, there are a few proposed techniques for addressing this problem.<sup>40–42</sup> However, these effects are exceedingly small under the hot, compressed conditions studied here. We obtained excellent agreement between DFTB and DFT for the  $\text{H}_2\text{O}_2$  pressure–volume relation at 0 K up to 40 GPa (Figure 2). The starting configuration for our geometry optimizations was taken from an NVT simulation with DFT at 300 K and 1.45 g/cm<sup>3</sup> (the experimental density). Optimization with DFT to zero pressure yielded a density of 1.47 g/cm<sup>3</sup>, whereas results from both DFT with dispersion

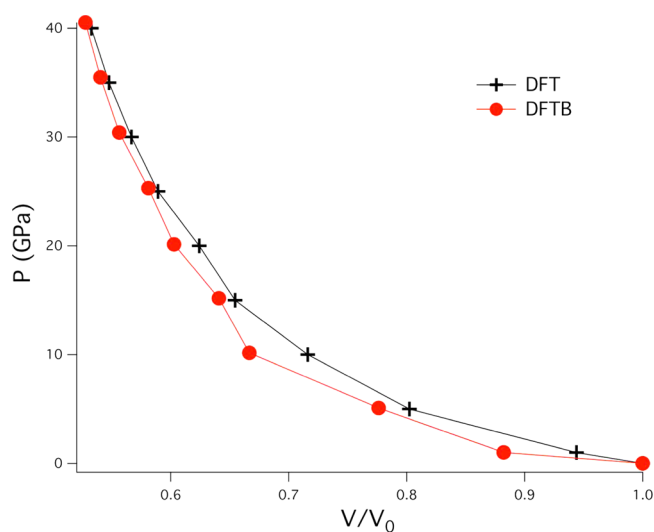


**Figure 2.** Comparison of the 0 K pressure–volume curves for DFT vs DFTB up to 40 GPa.

corrections and our DFTB calculations yielded a density of 1.56 g/cm<sup>3</sup>.

To perform simulations of the unique thermodynamic conditions of a shock,<sup>5</sup> we use the Multiscale Shock compression Simulation Technique (MSST).<sup>43</sup> MSST is a simulation methodology based on MD and the Navier–Stokes equations for compressible flow. Instead of simulating a planar shock wave within a large computational cell with many atoms, the MSST computational cell follows a Lagrangian point through the shock wave. MSST has been shown to accurately reproduce the shock Hugoniot (thermodynamic end states) of a number of systems<sup>5,15,30</sup> as well as the sequence of thermodynamic states throughout the reaction zone of shock compressed explosives, and the same shock wave profiles, physics, and chemistry found in direct, multimillion particle simulation of shock compression. The same computational and analysis procedures used in this study have been applied (and are fully described) in previous work.<sup>5,6,15,30,43,44</sup> New MSST equations of motion used in this study allow for a self-consistent dynamic electron temperature, where the ionic and electronic temperatures are kept equal at all times.<sup>45</sup> Quantum nuclear vibrational effects are known to enhance chemical reactivity of hydrogen containing liquids at similar conditions.<sup>46,47</sup> However, here we consider classical ion dynamics, only.

We performed simulations at shock velocities between 3 and 10 km/s (corresponding to particle speeds ranging from  $\sim 0.5$ –5 km/s, which covered the experimental data at  $\sim 1.2$  and 2 km/s particle speed), and all simulations were run between 50 and 150 ps. An initial, preshock configuration was prepared by simulating 64  $\text{H}_2\text{O}_2$  in an orthorhombic simulation twice as long in the direction of the shock at 300 K for 10 ps at the experimental density of 1.45 g/mL, followed by a cell optimization to approximately zero pressure and simulation at 300 K for an additional 10 ps. Simulations with 128  $\text{H}_2\text{O}_2$  molecules at select shock velocities yielded an identical equation of state and time-scale for chemical reactivity, indicating the lack of system size effects in our simulations.

## 4. RESULTS

Typical examples of the raw phase shift data are shown in Figure 3, along with fits to the data which give shock parameters.<sup>16</sup> Fifty shots each are taken at three different pump energy/ablator thickness combinations. Each shot gives a data set similar to one of the three shown in Figure 3. Raw data from each shot are analyzed independently, giving an estimate of the piston speed and the shock wave speed for every shot. A compilation of the data in piston speed/shock speed space is shown in Figure 4. Each cluster of points corresponds to a different pump intensity/ablator thickness, where the “high” intensity used is  $\sim 10^{11}$  W/cm<sup>2</sup> (corresponding to  $\sim 100$   $\mu\text{J}$  pulse energy). “Low” intensity corresponds to a pulse energy 22% smaller than high intensity.

The initial wave from the piston is likely longer than the steady shock rise in the sample at the same final particle speed. Given the sound speed distribution in the sample, we can conservatively estimate the time required for the wave to fully steepen to be some 10s of ps (and certainly less than 100 ps) after injection into the sample for all data. Further unsteadiness in the thereafter fully steepened wave results from variation of the piston speed, and error in shock and piston speed estimates due to this effect is evaluated below. All data are fit at

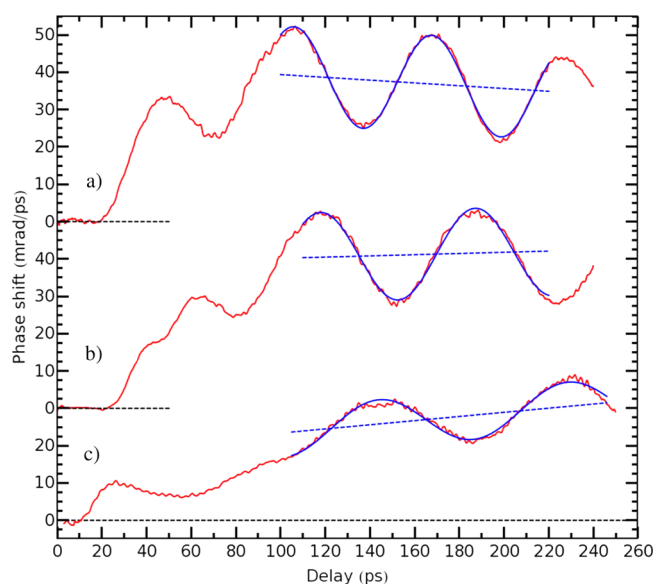


**Figure 3.** Examples of raw data sets, one from each cluster of data at the three different pump intensity/ablator thickness combinations, plotted along with fits: (a) high intensity, 1  $\mu\text{m}$  ablator; (b) low intensity, 1  $\mu\text{m}$  ablator; (c) low intensity, 2  $\mu\text{m}$  ablator. Black, dashed lines show the baseline for vertically offset data sets. Each data set is from a single shot, where the fit gives a particle and shock speed. Each cluster of speed data (shown in Figure 4) comprises 50 such data sets. The data are shown in red, the fit is shown in blue, and the linear offset part of the fit is shown as a blue dashed line. Each fit is shown over the fitting window that was used, and the same fitting window was used for all data sets in a given cluster of data.

sufficiently late times in the trace to assume a fully steepened wave over the fit window.

Exothermic chemistry between the shock front and the piston will accelerate material upstream (downstream) from the reaction zone in the direction of (opposite) the initial piston velocity, ultimately reducing the piston speed and increasing the speed of the lead shock. Any combination of a reduction in the piston speed and an increase in the shock wave speed will give a  $u_s-u_p$  point in the half-plane above the unreacted Hugoniot in  $u_s-u_p$  space, consistent with our observations.

Compressive strain rates were estimated from measured particle speeds in the current experiment and ultrafast experiments in our group, which directly measured the strain rate of the piston as a function of particle speed.<sup>10</sup> On the basis of these estimates, the strain rate at the piston was  $\approx 1.7 \times 10^{10} \text{ s}^{-1}$  for the 1  $\mu\text{m}$  ablator and  $\approx 10^{10} \text{ s}^{-1}$  for the 2  $\mu\text{m}$  ablator for the unreacted shots. Because the driving strain rate is monotonic with laser drive energy,<sup>10</sup> the driving strain rate at the piston for the reacted shots was larger than the strain rate for the unreacted shots.

The two (red and green) clusters of lower intensity shots match very well the shock Hugoniot (thermodynamic end states) of 90% hydrogen peroxide in the absence of chemical reactions, henceforth designated as unreacted Hugoniot (shown in Figure 4 by a dotted line), calculated using an exp6-polar model<sup>48</sup> for hydrogen peroxide, derived from measured sound speeds (Figure 4, inset) at high pressures (and further constrained by critical point<sup>49</sup> and dipole moment data<sup>50</sup>), as well as the “universal” liquid Hugoniot<sup>51</sup> for unreacted 90% hydrogen peroxide (shown in the figure by a dashed line).

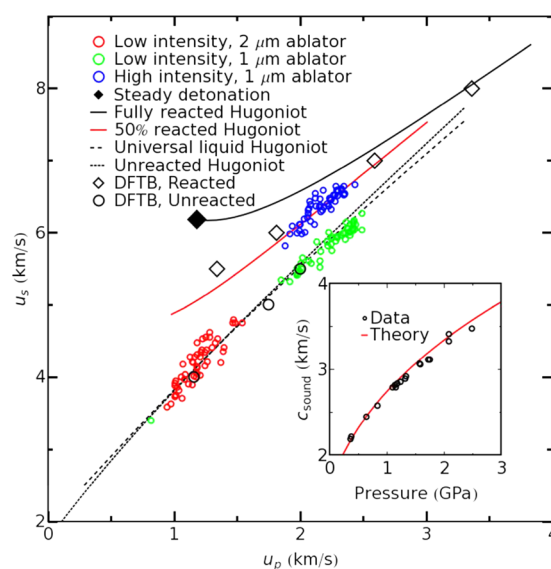


**Figure 4.** Piston and shock wave speeds for three different combinations of pump energy and ablator thickness. Also shown are a thermochemical calculation<sup>53</sup> for the 50% reacted Hugoniot (solid red line), unreacted Hugoniot derived from measured sound speeds (black dotted line), and the “universal” liquid Hugoniot<sup>51</sup> for  $\text{H}_2\text{O}_2$  (black dashed line). The solid black line is a thermochemical calculation of the fully reacted Hugoniot, and the black diamond specifies the steady-state detonation condition. Results for DFTB calculations are also shown. Sound speeds (black open circles) in unreacted  $\text{H}_2\text{O}_2$  at room temperature and high pressures, measured using impulsively stimulated light scattering (ISLS)<sup>28</sup> in a diamond anvil cell are shown in the inset. The sample is a solid at room temperature above approximately 2 GPa. The red line in the inset is a fit based on an exp6-polar model for liquid  $\text{H}_2\text{O}_2$ , similar to the one developed for water.<sup>48</sup> This sound speed calibrated model predicts the Hugoniot shown as a black dotted line in the main figure.

In contrast, the higher intensity shots (blue points in Figure 4) exhibit larger shock wave speeds for a given piston speed, consistent with shock induced chemistry occurring over the duration of the experiment. In particular, exothermic chemistry results in an increase in volume in the shock compressed sample due to the expanding hot, gaseous products (i.e.,  $\text{H}_2\text{O}$  and  $\text{O}_2$ ). This produces a higher shock wave speed than would be obtained if the material did not react. The higher intensity data agree very well with the partially (50%) reacted Hugoniot (in red) given by thermochemical calculations<sup>52</sup> based on exp6-polar modeling of the fluid mixture. Also shown in Figure 4 are similar calculations for the fully reacted Hugoniot (black line) and the steady-state detonation speed (black diamond); the latter matches very well available experimental results.<sup>53</sup> It is also worth noting that each of the higher intensity shots produces a bubble of gas in the shocked region, whereas nominally unreacted shots do not. It is very likely that they form as a result of the decomposition of hydrogen peroxide into water and gaseous molecular oxygen.

Via the analysis described in section 2e, deviations of estimated shock speeds due to variations in the offset are less than 2% for variations in the offset comparable to the higher piston speed clusters ( $u_p \sim 2 \text{ km/s}$ ) and less than 4% for variations in the offset comparable to the lower piston speed cluster. These errors are similar in magnitude to the scatter of the shock speed data, which has a standard deviation from a linear fit of less than 1.7% and 3.6% for the higher and lower

particle speed data sets, respectively. The lower piston speed data have a larger error due to the relatively large deviation from a constant in the offset compared to the higher piston speed data (Figure 3a,b vs Figure 3c). An analysis of the index of refraction using the Clausius–Mossotti relation indicates that, controlling for density, the variation of the index of refraction with composition (i.e., reactants vs products) is less than 1%, giving an error in the speed estimates of less than 1%.

Figure 5 shows the Hugoniot end states of Figure 4 in pressure–volume space, along with DFTB–MD simulation

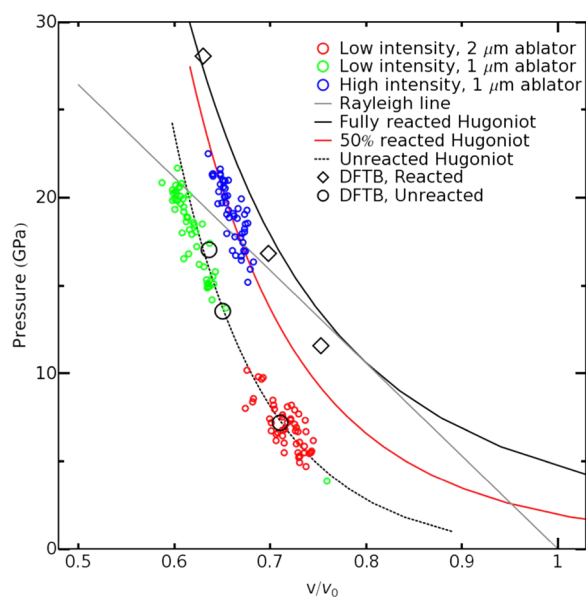


**Figure 5.** Thermodynamic states given by the measured particle and shock wave speeds of Figure 4. Specific volumes are normalized by the initial values. The style of lines and points are consistent with Figure 4. The open black symbols are results calculated using DFTB molecular dynamics simulations for pure  $\text{H}_2\text{O}_2$ , diamonds correspond to the reacted Hugoniot, and circles correspond to the unreacted Hugoniot. The Rayleigh line for 90%  $\text{H}_2\text{O}_2$  (detonation velocity 6.18 km/s) is shown in gray; it is tangent to the reacted Hugoniot at the Chapman–Jouguet point and it intersects the unreacted Hugoniot at the von Neumann spike.<sup>1</sup>

results for pure  $\text{H}_2\text{O}_2$ . Results from the DFTB simulations are in agreement with experimental data for both unreacted and reacted Hugoniot curves. The occurrence of chemistry, i.e.  $\text{H}_2\text{O}_2$  dissociation, and the extent of the chemical reaction were directly identified in the simulations by analyzing the molecular species concentration as a function of time.

Similar to previous work (see refs 30, 5, and 6), in our simulations we define molecular species by first choosing an optimal bonding cutoff  $r_c$  for all possible bonds. The optimal value for  $r_c$  to distinguish between bonded and nonbonded atomic sites is given by the first minimum in the corresponding pair radial distribution function  $g(R)$ , which corresponds to the maximum of the potential of mean force, viz.,  $W(R) = -k_B T \ln[g(R)]$ , for all possible bonding pairs. This choice corresponds to the optimal definition of the transition state within transition-state theory (see ref 6). In addition, to avoid counting species that are entirely transient and not chemically bonded (see ref 30), we also choose a lifetime cutoff of 50 fs. This criteria is intuitive because bonds with this lifetime could conceivably be detected spectroscopically. As a result, atom pairs are considered to be bonded only if they resided within a

distance of each other of  $r_c$  for a time of greater than 50 fs. Using these bonding criteria, specific molecular species are then defined by recursively creating a data tree of all atomic bonds branching from the original bonded pair. The chemical reactivity, concentrations, and lifetimes of different species are then determined by monitoring the creation and dissociation of specific molecules during the course of the simulations. Shorter and longer bond-lifetime criteria are also tested. The concentrations of species at high pressure and temperature have some dependence on bond and lifetime criteria, as expected, which has been shown for other hot dense materials (see refs 6 and 54). We found that the overall conclusions of this work are independent of the choice of bond and lifetime criteria.

The MD results show a transition from unreactive to reactive shocks as the shock velocity is increased (see Figure 5), with chemical reactions occurring on time scales of roughly 100 ps (Figure 6). The product species found for the reactive shocks

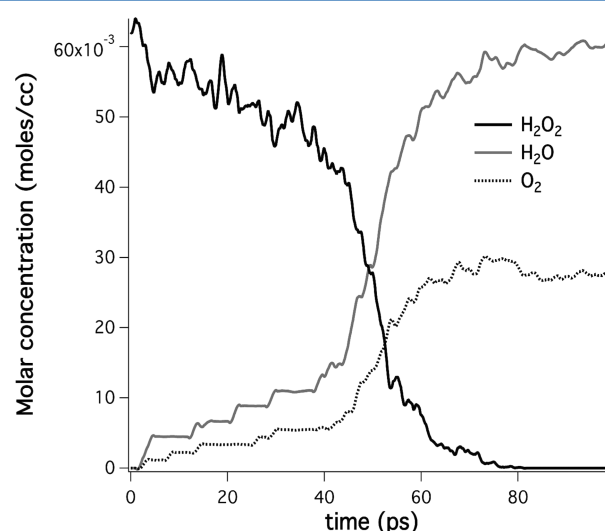


**Figure 6.** Mole concentrations of reactants and products from DFTB simulations at close to detonation conditions (shock velocity of 5.5 km/s) in pure hydrogen peroxide, where time is measured from the arrival of the lead shock in a given parcel of unreacted material.

are primarily  $\text{H}_2\text{O}$  and  $\text{O}_2$ , with negligible amounts of other molecules, including monatomic hydrogen and oxygen. We note that although in the experiments the nominally reacted shots do not appear to reach steady-state hydrodynamic conditions (consistent with a detonation wave), they are clearly consistent with chemical reactions occurring on time scales comparable to the simulation results. Future modeling of the entire experimental setup using hydrodynamics/reaction coupling at the continuum scale may enable the direct determination of chemical reaction rates from the experimental results.

We note that the measured particle speeds of one unreacted cluster of shots (at 2 km/s particle speed) are larger than the particle speed corresponding to the steady-state detonation (the black diamond in Figure 4 and refs 2 and 53) threshold. This likely indicates that shock induced reactions in unreacted data are kinetically limited on the time scale of the present experiment. Previous longer time scale experimental results on hydrogen peroxide have shown that just above the detonation threshold ( $\approx 13.3 \text{ GPa}^2$ ) the formation of a detonation wave occurs at least  $\sim 1 \mu\text{s}^2$  subsequent to shock compression. We



also find that the high intensity data are consistent with a partially reacted Hugoniot (Figure 5), likely because the compression wave does not evolve to a steady-state detonation over the duration of the experimental window.

Longer time scale experiments at shock pressures just above the detonation threshold have indicated propagation of a shock front well into the sample without reaction, followed by the initiation of reactions at the piston, and the propagation of a “superdetonation” reaction front from the piston to the shock front.<sup>55</sup> In the present work, observation of reactions within 100 ps of shock arrival in the sample indicates prompt reaction behind the shock front, with a time scale for complete reaction comparable to the  $\sim 100$  ps time scales observed in our MD simulations (Figure 6). Further, we observe both reacted and unreacted states at similar pressures (Figure 5), indicating that reactivity is not a function of pressure only, in this regime (i.e., near  $\sim 2$  km/s piston speed). This suggests that an alternate mechanism modulates the onset of chemical reactivity at these pressures (and corresponding piston speeds), and a strain rate dependent initiation mechanism is a plausible candidate. Such a mechanism is different from standard chemical kinetics, depending only on local thermodynamic variables, which is, for example, conventionally employed in phenomenological models of chemically reacting shock waves.<sup>2,13,55</sup>

## 5. CONCLUSIONS

The observation of chemical reactions just above the shock initiation threshold requires incubation times on the order of microseconds,<sup>2,55</sup> where homogeneous nucleation-like initiation of chemical reactions occurs in the compressed material behind the initial unreactive shock. The results summarized here indicate that ultrafast drives can be used to control compression induced exothermic chemical reactivity on much shorter time scales, consistent with those of MD simulations. We also suggest that strain rate dependent initiation is a plausible candidate to explain the modulation of reactivity we observe at similar pressures in shocked hydrogen peroxide. Shock-induced chemistry experiments with picosecond time resolution, as demonstrated here, afford the observation and control of reactivity over ultrafast time scales and may ultimately enable new nanoscale material synthesis methods.<sup>56</sup>

## AUTHOR INFORMATION

### Corresponding Author

\*M. R. Armstrong: e-mail, armstrong30@llnl.gov.

### Author Contributions

<sup>†</sup>Equal contributor to first author. E-mail: zaug1@llnl.gov

### Notes

The authors declare no competing financial interest.

## ACKNOWLEDGMENTS

<sup>6</sup>We acknowledge useful conversations with L. E. Fried, S. McGrane, C. Tarver, and R. Manaa. We also recognize the friendship and achievements of W. Michael Howard, who will be greatly missed. This research was performed under the auspices of the U.S. Department of Energy by Lawrence Livermore National Laboratory under Contract No. DE-AC52-07NA27344, and it was funded by Laboratory Directed Research and Development grant 11ERD067 with S.B. as principal investigator.

## REFERENCES

- (1) Zeldovich, I. B. *Theory of Detonation*; Academic Press: New York and London, 1960.
- (2) Sheffield, S. A.; Dattlebaum, D. M.; Stahl, D. B.; Gibson, L. L.; Bartram, B. D.; Engelke, R. Shock Initiation and Detonation Study on High Concentration  $\text{H}_2\text{O}_2/\text{H}_2\text{O}$  Solutions Using In-Situ Magnetic Gauging. *Proceedings of the 14th International Detonation Symposium* **2010**, 601–610.
- (3) Mochalin, V. N.; Shenderova, O.; Ho, D.; Gogotsi, Y. The Properties and Applications of Nanodiamonds. *Nat. Nanotechnol.* **2012**, 7, 11–23.
- (4) Qu, Y.; Li, X.; Wang, X.; Liu, D. Detonation Synthesis of Nanosized Titanium Dioxide Powders. *Nanotechnology* **2007**, 18, 205602.
- (5) Reed, E. J.; Manaa, M. R.; Fried, L. E.; Glaesemann, K. R.; Joannopoulos, J. D. A Transient Semimetallic Layer in Detonating Nitromethane. *Nat. Phys.* **2008**, 4, 72–76.
- (6) Wu, C. J.; Fried, L. E.; Yang, L. H.; Goldman, N.; Bastea, S. Catalytic Behaviour of Dense Hot Water. *Nat. Chem.* **2009**, 1, 57–62.
- (7) Radulescu, M. I.; Tang, J. Nonlinear Dynamics of Self-Sustained Supersonic Reaction Waves: Fickett's Detonation Analogue. *Phys. Rev. Lett.* **2011**, 107, 164503.
- (8) McGrane, S. D.; Moore, D. S.; Funk, D. J. Shock Induced Reaction Observed via Ultrafast Infrared Absorption in Poly(vinyl Nitrate) Films. *J. Phys. Chem. A* **2004**, 108, 9342–9347.
- (9) Nellis, W. J. Dynamic Compression of Materials: Metallization of Fluid Hydrogen at High Pressures. *Rep. Prog. Phys.* **2006**, 69, 1479–1580.
- (10) Crowhurst, J. C.; Armstrong, M. R.; Knight, K. B.; Zaug, J. M.; Behymer, E. M. Invariance of the Dissipative Action at Ultrahigh Strain Rates Above the Strong Shock Threshold. *Phys. Rev. Lett.* **2011**, 107, 144302.
- (11) Gilman, J. J. Mechanochemistry. *Science* **1996**, 274, 65–65.
- (12) Gilman, J. J. Chemical Reactions at Detonation Fronts in Solids. *Philos. Mag. Part B* **1995**, 71, 1057–1068.
- (13) Kirkwood, J.; Wood, W. Structure of a Steady-State Plane Detonation Wave with Finite Reaction Rate. *J. Chem. Phys.* **1954**, 22, 1915–1919.
- (14) Gibson, L. L.; Bartram, B.; Dattlebaum, D. M.; Sheffield, S. A.; Stahl, D. B. A Remote Liquid Target Loading System for a Two-Stage Gas Gun. In *Shock Compression of Condensed Matter - 2009, Pts 1 and 2*; Elert, M. L.; Buttler, W. T.; Furnish, M. D.; Anderson, W. W.; Proud, W. G., Eds.; American Institute of Physics: Melville, PA, 2009; Vol. 1195, pp 133–136.
- (15) Goldman, N.; Reed, E. J.; Kuo, I.-F. W.; Fried, L. E.; Mundy, C. J.; Curioni, A. Ab Initio Simulation of the Equation of State and Kinetics of Shocked Water. *J. Chem. Phys.* **2009**, 130, 124517.
- (16) Armstrong, M. R.; Crowhurst, J. C.; Bastea, S.; Zaug, J. M. Ultrafast Observation of Shocked States in a Precompressed Material. *J. Appl. Phys.* **2010**, 108, 023511.
- (17) Bolme, C. A.; McGrane, S. D.; Moore, D. S.; Funk, D. J. Single Shot Measurements of Laser Driven Shock Waves Using Ultrafast Dynamic Ellipsometry. *J. Appl. Phys.* **2007**, 102, 033513.
- (18) Benuzzi-Mounaix, A.; Koenig, M.; Boudenne, J. M.; Hall, T. A.; Batani, D.; Scianitti, F.; Masini, A.; Di Santo, D. Chirped Pulse Reflectivity and Frequency Domain Interferometry in Laser Driven Shock Experiments. *Phys. Rev. E* **1999**, 60, R2488–R2491.
- (19) Evans, R.; Badger, A. D.; Falliès, F.; Mahdih, M.; Hall, T. A.; Audebert, P.; Geindre, J.-P.; Gauthier, J.-C.; Mysyrowicz, A.; Grillon, G.; et al. Time- and Space-Resolved Optical Probing of Femtosecond-Laser-Driven Shock Waves in Aluminum. *Phys. Rev. Lett.* **1996**, 77, 3359.
- (20) Patterson, J. E.; Lagutchev, A.; Huang, W.; Dlott, D. D. Ultrafast Dynamics of Shock Compression of Molecular Monolayers. *Phys. Rev. Lett.* **2005**, 94, 015501.
- (21) Zel'dovich, B. Y.; Raizer, Y. P. *Physics of Shock Waves and High-temperature Hydrodynamic Phenomena*; Reprod.; Dover Publications: Mineola, NY, 2002.



- (22) McGrane, S. D.; Moore, D. S.; Funk, D. J.; Rabie, R. L. Spectrally Modified Chirped Pulse Generation of Sustained Shock Waves. *Appl. Phys. Lett.* **2002**, *80*, 3919–3921.
- (23) Giguere, P.; Geoffrion, P. Changes of Density of Hydrogen Peroxide Solutions on Cooling and Freezing. *Can. J. Res. Sect. B-Chem. Sci.* **1950**, *28*, 599–607.
- (24) Gardner, D.; Michalka, T.; Saraswat, K.; Barbee, T.; Mcvittie, J.; Meindl, J. Layered and Homogeneous Films of Aluminum and Aluminum Silicon with Titanium and Tungsten for Multilevel Interconnects. *IEEE Trans. Electron Devices* **1985**, *32*, 174–183.
- (25) Gardner, D. S.; Saraswat, K. C.; Barbee, T. W., Jr. U.S. Patent No. 4673623, 1983.
- (26) Armstrong, M. R.; Crowhurst, J. C.; Bastea, S.; Howard, W. M.; Zaug, J. M.; Goncharov, A. F. Prospects for Achieving High Dynamic Compression with Low Energy. *Appl. Phys. Lett.* **2012**, *101*, 101904.
- (27) Nichols, A. L. *Users Manual for ALE3D, LLNL Technical Report LLNL-SM-433954*; LLNL Technical Report LLNL-SM-433954; Lawrence Livermore National Laboratory: Livermore, CA, 2010.
- (28) Zaug, J.; Slutsky, L.; Brown, J. Equilibrium Properties and Structural Relaxation in Methanol to 30.4 GPa. *J. Phys. Chem.* **1994**, *98*, 6008–6016.
- (29) Datchi, F.; LeToullec, R.; Loubeyre, P. Improved Calibration of the SrB<sub>4</sub>O<sub>7</sub>:Sm<sup>2+</sup> Optical Pressure Gauge: Advantages at Very High Pressures and High Temperatures. *J. Appl. Phys.* **1997**, *81*, 3333–3339.
- (30) Goldman, N.; Reed, E. J.; Fried, L. E.; Kuo, I.-F. W.; Maiti, A. Synthesis of Glycine-containing Complexes in Impacts of Comets on Early Earth. *Nat. Chem.* **2010**, *2*, 949–954.
- (31) Kohn, W.; Sham, L. J. Self-Consistent Equations Including Exchange and Correlation Effects. *Phys. Rev.* **1965**, *140*, A1133–A1138.
- (32) Manaa, M. R.; Fried, L. E.; Melius, C. F.; Elstner, M.; Frauenheim, T. Decomposition of HMX at Extreme Conditions: A Molecular Dynamics Simulation. *J. Phys. Chem. A* **2002**, *106*, 9024–9029.
- (33) Reed, E. J.; Fried, L. E.; Henshaw, W. D.; Tarver, C. M. Analysis of Simulation Technique for Steady Shock Waves in Materials with Analytical Equations of State. *Phys. Rev. E* **2006**, *74*, 056706.
- (34) Aradi, B.; Hourahine, B.; Frauenheim, T. DFTB+, a Sparse Matrix-based Implementation of the DFTB Method. *J. Phys. Chem. A* **2007**, *111*, 5678–5684.
- (35) Plimpton, S. J. *Comput. Phys.* **1995**, *117*, 1.
- (36) VandeVondele, J.; Krack, M.; Mohamed, F.; Parrinello, M.; Chassaing, T.; Hutter, J. QUICKSTEP: Fast and Accurate Density Functional Calculations Using a Mixed Gaussian and Plane Waves Approach. *Comput. Phys. Commun.* **2005**, *167*, 103–128.
- (37) Goedecker, S.; Teter, M.; Hutter, J. Separable Dual-space Gaussian Pseudopotentials. *Phys. Rev. B* **1996**, *54*, 1703–1710.
- (38) Lee, C.; Yang, W.; Parr, R. Development of the Colle-Salvetti Correlation-Energy Formula into a Functional of the Electron-Density. *Phys. Rev. B* **1988**, *37*, 785–789.
- (39) Becke, A. Density-Functional Exchange-Energy Approximation with Correct Asymptotic-Behavior. *Phys. Rev. A* **1988**, *38*, 3098–3100.
- (40) Goerigk, L.; Grimme, S. Assessment of TD-DFT Methods and of Various Spin Scaled CIS(D) and CC2 Versions for the Treatment of Low-lying Valence Excitations of Large Organic Dyes. *J. Chem. Phys.* **2010**, *132*, 184103.
- (41) Jurečka, P.; Černý, J.; Hobza, P.; Salahub, D. R. Density Functional Theory Augmented with an Empirical Dispersion Term. Interaction Energies and Geometries of 80 Noncovalent Complexes Compared with Ab Initio Quantum Mechanics Calculations. *J. Comput. Chem.* **2006**, *28*, 555–569.
- (42) Tkatchenko, A.; Scheffler, M. Accurate Molecular Van Der Waals Interactions from Ground-State Electron Density and Free-Atom Reference Data. *Phys. Rev. Lett.* **2009**, *102*, 073005.
- (43) Reed, E. J.; Fried, L. E.; Joannopoulos, J. D. A Method for Tractable Dynamical Studies of Single and Double Shock Compression. *Phys. Rev. Lett.* **2003**, *90*, 235503.
- (44) Reed, E. J.; Rodriguez, A. W.; Manaa; Fried, L. E. Tarver Ultrafast Detonation of Hydrazic Acid (HN<sub>3</sub>). *Phys. Rev. Lett.* **2012**, *109*, 038301.
- (45) Reed, E. J. Electron-Ion Coupling in Shocked Energetic Materials. *J. Phys. Chem. C* **2012**, *116*, 2205–2211.
- (46) Qi, T.; Reed, E. J. Simulations of Shocked Methane Including Self-Consistent Semiclassical Quantum Nuclear Effects. *J. Phys. Chem. A* **2012**, *116*, 10451–10459.
- (47) Goldman, N.; Reed, E. J.; Fried, L. E. Quantum Mechanical Corrections to Simulated Shock Hugoniot Temperatures. *J. Chem. Phys.* **2009**, *131*.
- (48) Bastea, S.; Fried, L. E. Exp6-polar Thermodynamics of Dense Supercritical Water. *J. Chem. Phys.* **2008**, *128*, 174502.
- (49) Nikitin, E. D.; Pavlov, P. A.; Popov, A. P.; Nikitina, H. E. Critical Properties of Hydrogen Peroxide Determined from Direct Measurements. *J. Chem. Thermodyn.* **1995**, *27*, 945–952.
- (50) Cohen, E. A.; Pickett, H. M. The Dipole Moment of Hydrogen Peroxide. *J. Mol. Spectrosc.* **1981**, *87*, 582–583.
- (51) Woolfolk, R. W.; Cowperthwaite, M.; Shaw, R. A. "Universal" Hugoniot for Liquids. *Thermochim. Acta* **1973**, *5*, 409.
- (52) Bastea, S.; Fried, L. E. Chemical Equilibrium Detonation. In *Shock Wave Science and Technology Reference Library*; Springer: Berlin, 2012; Vol. 6, p 1.
- (53) Engelke, R.; Sheffield, S. A.; Davis, L. L. Experimental and Predicted Detonation Parameters for Liquid-phase H<sub>2</sub>O<sub>2</sub>/H<sub>2</sub>O Mixtures. *J. Phys. Chem. A* **2000**, *104*, 6894–6898.
- (54) Brenner, D.; Robertson, D.; Elert, M.; White, C. Detonations at Nanometer Resolution Using Molecular-Dynamics. *Phys. Rev. Lett.* **1993**, *70*, 2174–2177.
- (55) Hardesty, D. R. An Investigation of the Shock Initiation of Liquid Nitromethane. *Combust. Flame* **1976**, *27*, 229–251.
- (56) Vailionis, A.; Gamaly, E. G.; Mizeikis, V.; Yang, W.; Rode, A. V.; Juodkakis, S. Evidence of Superdense Aluminium Synthesized by Ultrafast Microexplosion. *Nat. Commun.* **2011**, *2*, 1.